JTTEE5 16:118–127
DOI: 10.1007/s11666-006-9003-6
1059-9630/$19.00 © ASM International

Peer Reviewed

Properties of Induction Plasma Sprayed Iron Based Nanostructured Alloy Coatings for Metal Based Thermal Barrier Coatings

Dong-il Shin, François Gitzhofer, and Christian Moreau

(Submitted October 20, 2005; in revised form December 28, 2005)

Metal-based thermal barrier coatings (MBTBCs) have been produced using high frequency induction plasma spraying (IPS) of iron-based nanostructured alloy powders. The study of MBTBCs has been initiated to challenge issues associated with current TBC materials such as difficult prediction of their "in-service" lifetime. Reliability of TBCs is an important aspect besides the economical consideration. Therefore, the study of MBTBCs, which should posses higher toughness than the current TBC materials, has been initiated to challenge the mechanical problems of ceramic-based TBCs (CBTBCs) to create a new generation of TBCs. The thermal diffusivity (TD) (α) properties of the MBTBCs were measured using a laser flash method, and density (ρ) and specific heat (C_p) of the MBTBCs were also measured for their thermal conductivity (k) calculation ($k = \alpha\rho C_p$).

Keywords amorphous/nanostructure, metal-based thermal barrier coatings (MBTBCs), phonon scattering

1. Introduction

Over the last two decades, thermal barrier coatings (TBCs) technologies have been enormously improved and enhanced by many researchers. Yttria stabilized zirconia (YSZ) has one of the lowest thermal conductivities (TC) about 2 W/mK, along with one of the highest expansion coefficients for a ceramic material (9.5×10^{-6}/K) being close to those of metals. Therefore, YSZ is widely used as a thermal insulator at elevated temperatures (Ref 1). One application for YSZ is thermally sprayed TBCs which are aimed to protect and insulate the hot section of metal components of advanced gas-turbines or internal combustion engines and have TC values of less than 1 W/mK (Ref 2). The use of TBCs can result in a temperature reduction of as much as 200 °C at the metal surface, thereby improving the durability of the metal component as well as enhancing the fuel efficiency (Ref 3). However, TBCs using the traditionally employed ceramic materials, such as YSZ, have a very difficult life-time prediction assessment because of their inherent brittle behavior. Therefore, a new concept of metal-based TBCs (MBTBCs) has been devised and is now considered appropriate for a new generation of TBCs. However, the MBTBCs have certainly a lower in-service temperature limit (around 500 °C) than ceramics due to phase change, grain growth, etc. (Ref 4). Therefore, the MBTBCs are appropriate only for certain application such as gasoline engines.

For the MBTBCs, it is very important to consider the free electron contributions to thermal conductivity because most of the metallic based materials are very electrically and thermally conductive, due to the existence of free electrons and phonons propagation at the atomic scale. The basic relationship between thermal conductivity k and a corresponding mean free path ℓ, for either electrons or phonons, can be defined as $k = 1/3C\upsilon\ell$ (Ref 1). The main focus of this study is how k can be minimized by reducing the mean free path. One of the theoretical approaches to the reduction of ℓ is to engineer defects into the material to hinder the mobility of electrons or phonons in the system for electron/phonon scatterings. For instance, different imperfections scatter phonons with different frequency dependence. High frequency phonons, which have wavelengths of the order of atomic dimensions, are scattered by point defects, while grain boundaries scatter low frequency phonons, and therefore their mean free path is comparable to the material grain size (Ref 5-9). In particular, Yang (Ref 10) has reported that a strong, grain-size-dependent, reduction in thermal conductivity is observed at temperatures from 6 to 480 K. The thermal conductivity of YSZ with a 10 nm grain size is reduced by more than a factor of two compared to that of much coarser-grained coatings. However, the grain size effect is smaller with increasing temperature (Ref 7).

In this work, MBTBCs were plasma-sprayed from iron-based alloy powders using induction plasma spraying (IPS) (Ref 4). The powder used is a commercially available iron based alloy material by the Nanosteel company (SHS717™), which is made from metal alloys in the

D. Shin and **F. Gitzhofer,** Centre de Recherche Energy, Plasma, and Electrochimique (CREPE) in Department of Chemical Engineering, Université de Sherbrooke, Sherbrooke, QC, Canada J1K2R1; and **C. Moreau,** Industrial Materials Institute, National Research Council of Canada, Boucherville, QC, Canada J4B6Y4. Contact e-mail: dong-il.shin@tekna.com

composition of Fe-25Cr-8Mo-10W-5Mn-5B-2C-2Si in wt%, with a particle size distribution was $d_{10\%}$ = 17 μm, $d_{50\%}$ = 23 μm, and $d_{90\%}$ = 45 μm. The basis of choosing the material is that it has a thermal conductivity of 5-6 W/mK (Ref 11) as a bulk material. With thermally sprayed coatings of the material, we expect the conductivity could reach much lower than 5 or 6 W/mK. The thermal conductivity of the coating ''as sprayed'' using the powder was calculated, from measurement of the density (ρ), specific heat (C_p), and thermal diffusivity (TD) (α). Crystal structure and phases in MBTBCs were characterized by Transmission Electron Microscopy (TEM) and x-ray diffraction (XRD), respectively.

2. Description of Experiments

2.1 Coating Production

Scanning electron microscopy (SEM, JEOL JSM-840A/Hitachi S4700 Cold Field Emission) images of the powder in the as-received condition are presented in Fig. 1. Nanostructured features are observable in the cross section of an individual powder, and they are in the size range between 50 and 150 nm. The powder was injected into Ar-N_2 or Ar-O_2 plasma, formed using a high frequency induction plasma torch (PL-50, TEKNA Plasma System Inc.). IPS parameters were optimized to get a lower thermal conductivity of MBTBCs.

The optimization of IPS parameters was performed with a method of analysis of variance (ANOVA). The purpose of ANOVA is to find out the sensitivity of IPS parameters on porosity of coatings because porosity is one of the major factors to be controlled for lower thermal conductivity in plasma-sprayed coatings. The three independent variables, used as spraying parameters, that have been considered are induction plasma torch power (kW), spray distance (mm) and N_2 vol.% in the plasma sheath gas, associated with the use of a TEKNA PL-50 induction plasma torch (TEKNA Plasma Systems, Sherbrooke, Québec). The level of each factor employed is presented in Table 1. The major objective of the optimization is the study of factors that have the strongest effects on porosity variation in the produced coatings. Design of the experiment is based on one half fraction of the 2^{X-1} design, with the defining relation of I = ABC. To construct the design, the basic design should be set as a $2^{3-1} = 2^2$ design, with the three independent variables, the level of the third factor C being found by solving I = ABC for C. The response of the design is set as the porosity. Rather than using N_2 as a sheath gas, O_2 gas was also used for a study of reactive plasma spraying, which is one of the major benefit of using RF induction plasma spraying techniques.

Table 1 ANOVA of two levels of the selected three factors

	Factor		
Levels	**A: Power, kW**	**B: Spraying distance, mm**	**C: N_2, vol.%**
+	45	150	80
−	24	270	20

In-flight particle characterization was also carried out to determine in-situ processing conditions of IPS parameters using a DPV2000 in-flight particle diagnostic system (Ref 12) (Tecnar Automation, St-Bruno, Quebec, Canada). The mean temperature and velocity were measured taking into account only particles in the range from 20 to 40 μm to avoid biassing the results due to the detectivity limit of the system (Ref 13).

2.2 Coating Characterization

The XRD technique was used to perform phase identification and grain size calculation of the coatings using an X-ray diffractometer (Philips X'pert Pro diffractometer). XRD techniques with Scherrer equation were also used to estimate the average grain size in the sprayed coatings, using the FWHM (full width at half maximum) values obtained from the XRD patterns of the coatings (Ref 14, 15). Oxygen/nitrogen content analysis was performed by using a TC500C Nitrogen/Oxygen Determinator (LECO Corporation). SEM was used to observe coating's structure and porosity in backscattered electron mode on a micro polished cross section of the coatings. Transmission electron microscopy (TEM, JEOL JEM 2100M) was used to observe the crystal structure and nanostructured grain sizes. Samples were sliced with a focussed ion beam

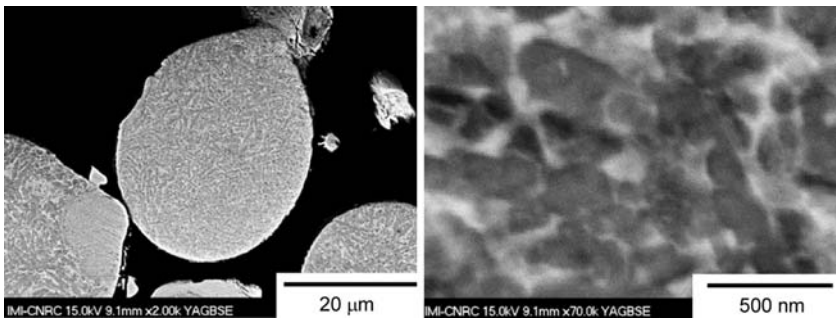

Fig. 1 SEM images on a cross section of SHS717 as received powder

system (FIB, Hitachi FB2000A) into to have a width, length and thickness for $10 \times 8 \times 0.2$ μm, respectively. The identified crystal structure and gain size measured by TEM diffraction technique and image analysis, respectively, are used to confirm the data from the XRD technique. Coating porosity was measured by image analysis with 5 randomly taken SEM pictures from each sample at 500 times magnification. The apparent density (DN) of the sprayed coatings was measured by the Archimedes principle (Ref 16) based on the ASTM B31-93, C693-93, and D3800-99 testing methods (Ref 17-19). All samples were dried in a furnace for 24 h at 110 °C to evaporate any moisture in open pores of the coatings, and weighted for m_{dry}. The samples were then immersed in distilled water by vacuum impregnation to fill the open pores with the water. Then, Archimedes weight, m_{Arch}, was measured using a hydrostatic weighing system (Sartorius 6068, Sartorius GmbH, Germany) for the coating density calculation. Thermal diffusivity measurement of the coatings was carried out at room temperature by using the laser flash method (Ref 20). A 0.8 J YAG laser pulse (70 μs duration, 6 mm diameter) was used to heat the front coating surface, and the temperature of the rear surface was monitored using an infrared InSb detector. The infrared signal was digitized using a Nicolet 440 scope. Specific heat (C_p) of the coatings was also measured using the Q1000 Tzero™ DSC (Differential scanning calorimetry, TA Instruments, Delaware) at room temperature. Thermal conductivity (k) was calculated by use of the relationship $k = \alpha\rho C_p$. For study of anisotropic properties of MBTBCs, 1-cm thick coating was sprayed and transversally cut to measure its thermal diffusivity. Schematic description of the anisotropy measurement is presented in Fig. 2.

3. Results and Discussion

3.1 Selection of IPS Parameters

Induction plasma spraying parameters were selected after conducting the ANOVA, and the results are shown in Table 2. The factor effects are calculated using an experimental design software (Ref 21) and shown in Table 3. From the table, the most effective factors are found to be the spraying distance and the N_2 vol.% in the plasma sheath gas. The porosity range obtained in this study lies between 5 and 17%. With respect to the porosity range, the independent variables are optimized and listed in Table 4. The expected porosity is plotted in Fig. 3. Along with the optimized independent variables for N_2 plasma spraying, five different spraying parameters (S1-S5) are selected, as presented in Table 5.

As discussed, one of the major benefits of using IPS is the in-flight reactive spraying to be adopted. Additional phases in MBTBCs can be induced by the use of reactive spraying of nanostructured alloy powder with an O_2 gas mixture in the plasma gas. Three different O_2 vol.% in plasma gas and their corresponding spraying parameters (S6-S8) were selected arbitrarily and presented in Table 5.

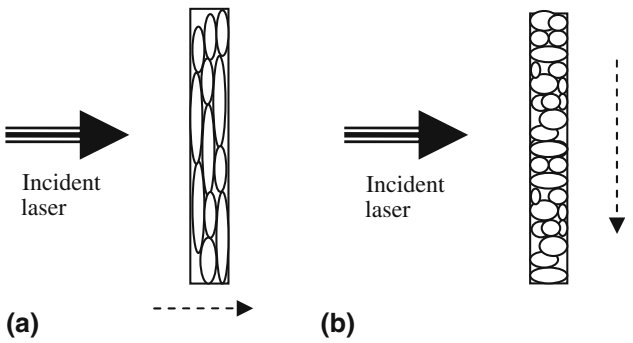

Fig. 2 Thermal diffusivity measurements: (a) PA direction: the incident laser is parallel to spraying direction; (b) PE direction: the incident laser is perpendicular to the spraying direction. The dotted arrows indicate the spraying direction

Table 2 The 2^{3-1} design with the defining relation I = ABC

Run order	Basic design A: Power	B: Spraying distance	C: N_2	Treatment combination	Porosity, %
1	+	+	+	ABC	17
2	−	−	+	C	7
3	+	−	−	A	5
4	−	+	−	B	10

Table 3 Factor effects

Code	Factor	Contribution %
A	Torch power	7.55
B	Spraying distance	67.98
C	N_2 vol.%	24.47

Table 4 Optimized independent parameters

Run number	Spraying distance, mm	N_2 vol.% in plasma sheath gas	Expected porosity, %
S1	150	80 (75 slpm)	12.7
S2	150	50 (47 slpm)	11.2
S3	150	20 (18 slpm)	10.2
S4	210	80 (75 slpm)	14.2
S5	270	80 (75 slpm)	15.5

4. Induction Plasma Sprayed MBTBCs with N_2 (IPS-N_2)

4.1 In-Flight Particle Characteristics

Studies on the in-flight particle temperature and velocity are presented in Fig. 4 and 5. The graphs reveal that average in-flight particle temperatures are in the range between 1800 and 2000 °C, which is higher than the

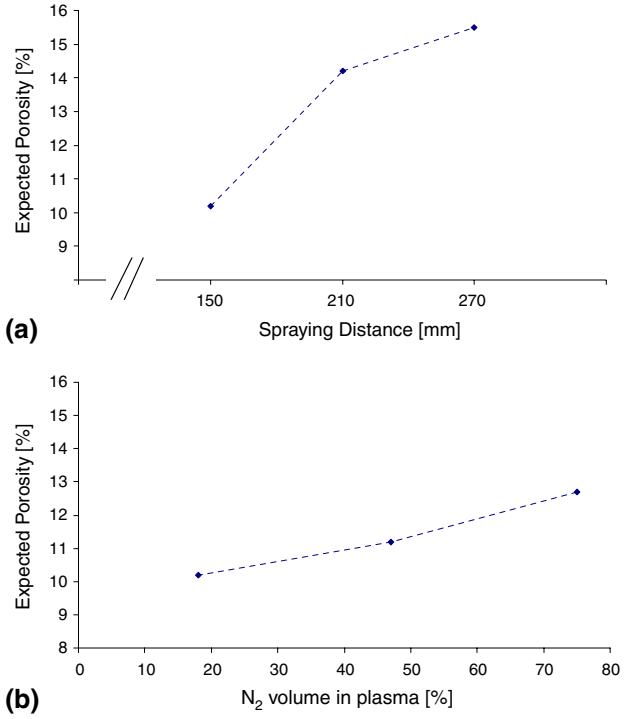

Fig. 3 Expected posity vs. spraying conditions: (a) spraying distance (mm) and (b) N_2 vol.% in plasma

Table 5 IPS spraying conditions

Parameters		S1	S2	S3	S4	S5	S6	S7	S8
Power, kW					24				
Feedrate, g/min					16				
Substrate cooling					Water				
Coating temperature controlled with					Liquid N_2				
Chamber pressure, Torr					100				
Spraying distance, mm		150	150	150	210	270	210		
Gas flow, slpm	Ar-sheath	18	46	75	75	75	75	62	45
	N_2-sheath	75	47	18	18	18			
	O_2-sheath						7	20	37
	Ar-central				23				
	Ar-carrier				4				

melting point of the Nanosteel powder, which is known as 1200 °C (Ref 22).

With increased N_2 partial pressure in the plasma gas, the in-flight particle temperature is increased by about 50 °C as shown in Fig. 4, while particle velocity remains between 42 and 45 m/s within the error of the 90% confidence level. Increasing particles temperature at the higher N_2 partial pressures can be explained by higher heat transfer coefficient due to N_2 vol.% increase in plasma.

As SD increases, the temperature decreases due to cooling of the in-flight particles as they exit from the IPS torch as presented in Fig. 5. Particle velocities versus SD change shows somewhat unusual behaviors, their velocities reaching maximum values at the spraying distance of

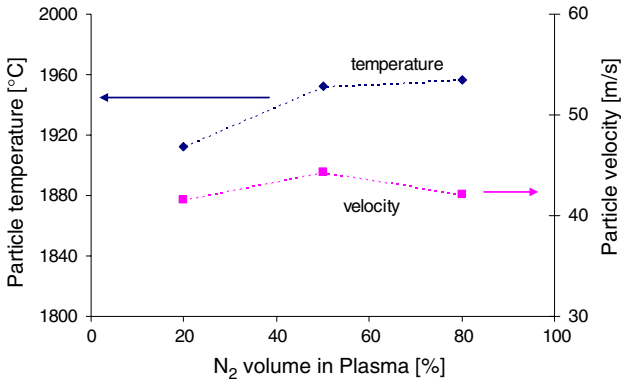

Fig. 4 In-flight particle temperature and velocity with different N_2 vol.% in the plasma for the selected particle size range between 20 and 40 μm

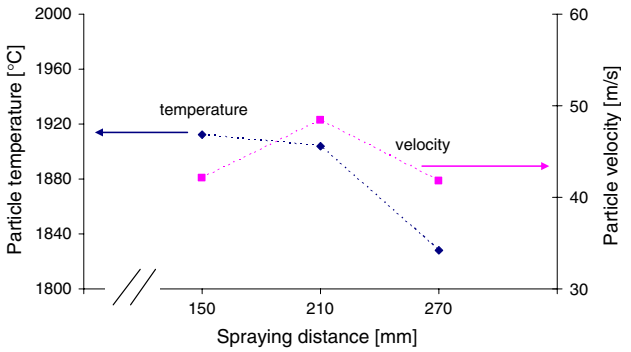

Fig. 5 In-flight particle temperature and velocity with spray distance change for the selected particle size range between 20 and 40 μm

~210 mm thereafter dropping to 270 mm. This behavior could be related to the acceleration and then deceleration of the particles as they are getting far away from the torch exit even though the variation is very small.

4.2 X-ray Diffraction

The XRD patterns set-out in Fig. 6 present that MBTBCs have fine nano or amorphous crystal structures. After spraying, crystal structure of the material has been changed from crystalline (as-received powder) to amorphous (as sprayed coating).

Along with the N_2 vol.% changes from 20 to 80 in the plasma gas and the spraying distance (SD) changes from 150 to 270 mm, the crystal structures of MBTBCs do not change significantly as can be seen in Fig. 6.

4.3 O_2/N_2 Contents

The result of the O_2/N_2 analysis is presented in Fig. 7. The N_2 wt% in the coatings tends to increase as a function of N_2 vol.% increase in plasma gas while O_2 wt% decreases. Higher N_2 partial pressure in plasma gas results in more nitrides formed or possible nitrogen solution in Fe with the maximum solubility of 0.1 wt% at 590 °C

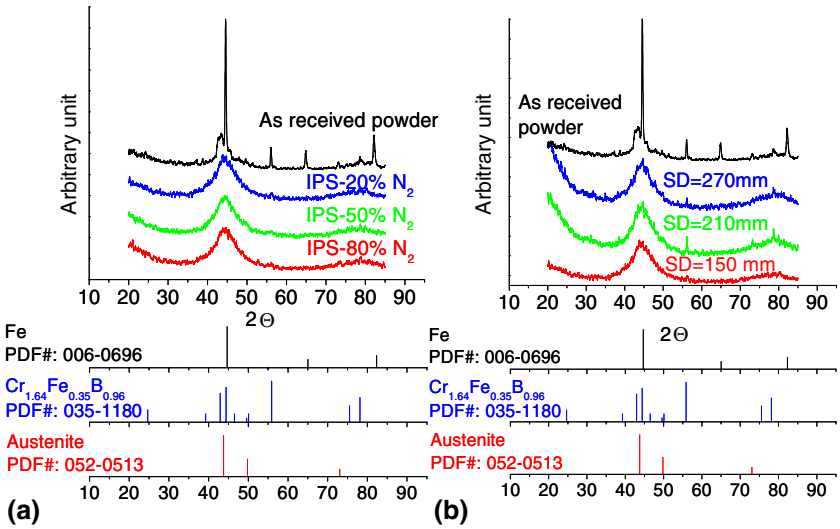

Fig. 6 XRD patterns of Nanosteel powder and the product MBTBCs sprayed with (a) N_2 vol.% change in plasma with SD = 150 mm, and (b) spraying distance (SD) change with IPS-20% N_2

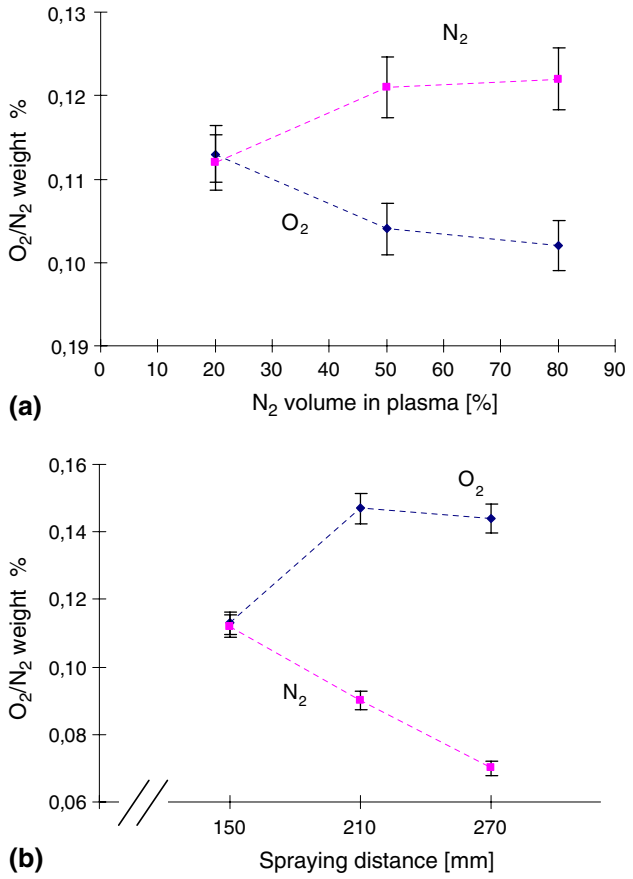

Fig. 7 O_2/N_2 wt% content in MBTBCs as a function of (a) N_2 vol.% in plasma with SD of 150 mm, (b) spraying distance with N_2 vol.% of 20

(Ref 23) in the coatings. Oxidation occurs due to residual oxygen present in IPS reactor and is promoted by longer dwelling time at a larger SD. N_2 wt% decreases because oxidation is the dominant reaction for Fe-based materials, which is in agreement with the free energy formation (Ref 24):

$$\Delta G_{Fe_4N} = 4\,\text{kJ/mol}, \quad \Delta G_{FeO} = 2,486\,\text{kJ/mol},$$
$$\Delta G_{Fe_2O_3} = 750\,\text{kJ/mol}, \quad \Delta G_{Fe_3O_4} = 1,015\,\text{kJ/mol}$$

4.4 Microstructure, Grain Size, and Porosity

TEM images shown in Fig. 8 confirm that as-sprayed MBTBCs are almost completely amorphous. These images were taken from a sample sprayed with IPS-20% N_2 and SD of 150 mm. The crystal structure consists of crystalline phases in an amorphous matrix. The amorphous structure in the MBTBCs can be explained by the quenching of fully molten particles from their hottest temperature (2000 °C) through the action of "flattening" onto the substrate surface. The crystalline phases are retained most likely from partially molten particles embedded into the coating. The grain size of MBTBCs, as measured by use of the Scherrer equation, is only a few nanometers, as presented in Fig. 9. In terms of changing the N_2 vol.% in the plasma gas and SD, grain sizes also tend to remain around 3 nm.

As illustrated in Fig. 10a, porosity increases with the N_2 vol.% as we expected from the optimization of spraying parameters (Table 5), which may be explained by a different wetting behavior of the molten particles impinging on the surface of the already deposited splats (Ref 15, 25). With respect to the results on in-flight particle characteristics, it is indeed very unusual that higher in-flight particle temperature yields higher porosity in coatings. However, the higher in-flight temperature can be explained by the higher heat transfer coefficient due to N_2 vol.% increase in plasma. In Fig. 10b, porosity change at the different spraying distances (SD) also resulted in more porous coating, corresponding to

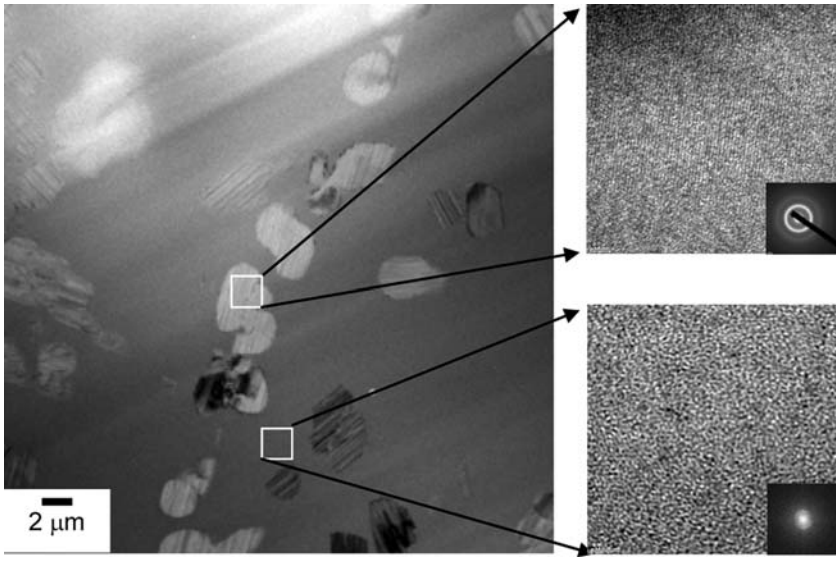

Fig. 8 TEM images on as-sprayed MBTBCs with IPS-20% N_2 and SD of 150 mm

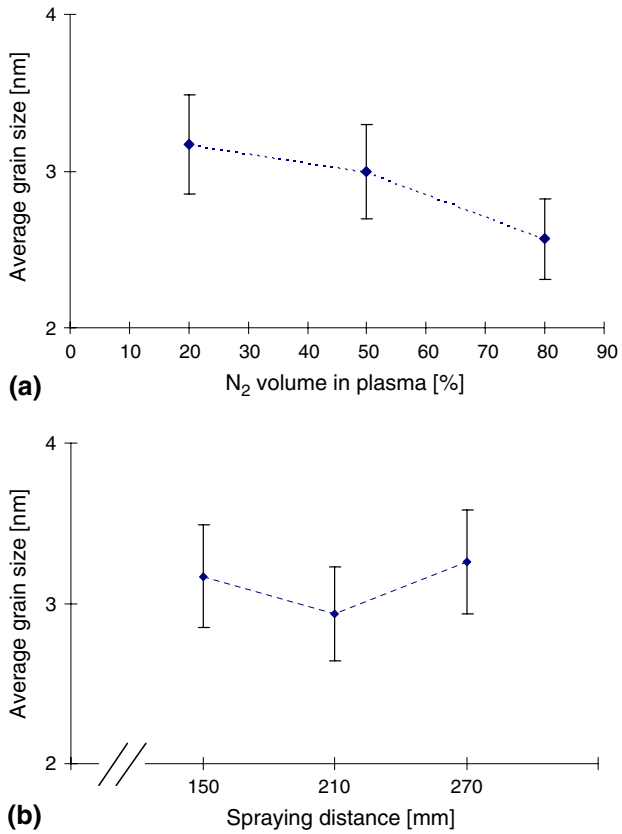

Fig. 9 Grain size change vs. (a) N_2 vol.% change in plasma, and (b) spraying distance change

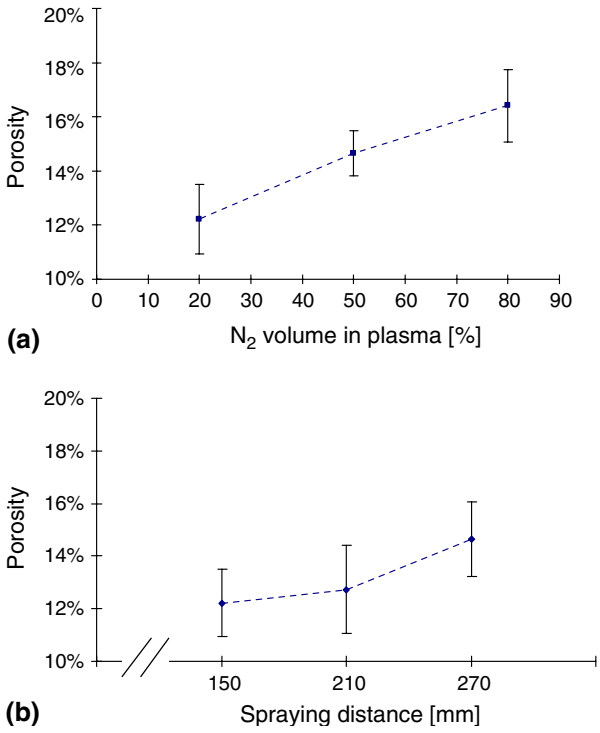

Fig. 10 Porosity changes vs. (a) various N_2 vol.% levels in plasma, and (b) spraying distance

the expected porosity from the optimization as presented in Table 5. In this case, porosity increase can be explained by the cooler spray particle temperatures existing at increased SD. As shown in Fig. 5, particle temperatures drop from around 1900 °C at a SD of 150 mm to around 1800 °C at a SD of 270 mm, which results in less particle flattening, and more porosity in the MBTBCs.

4.5 Thermal Diffusivity

In Fig. 11, the results on TD measurements show that N_2 vol.% change does not affect significantly TD of

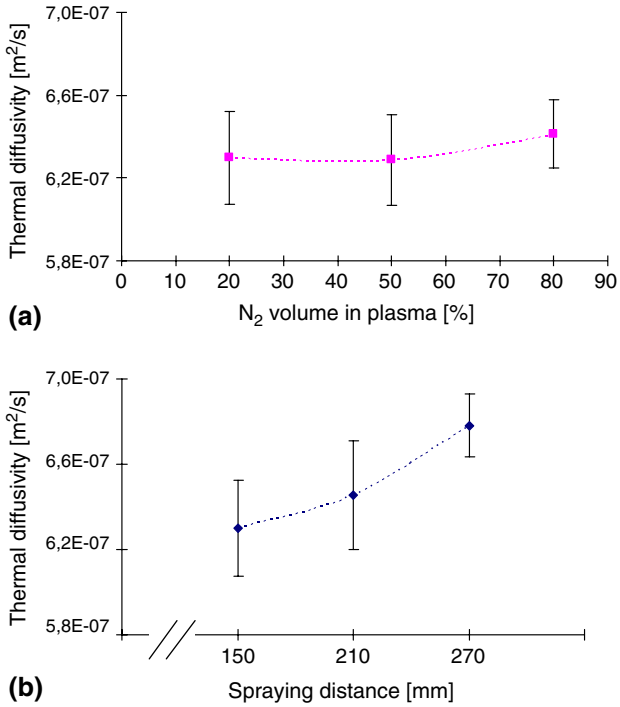

Fig. 11 Thermal diffusivity changes as a function of (a) N_2 vol.% in plasma, and (b) spraying distance

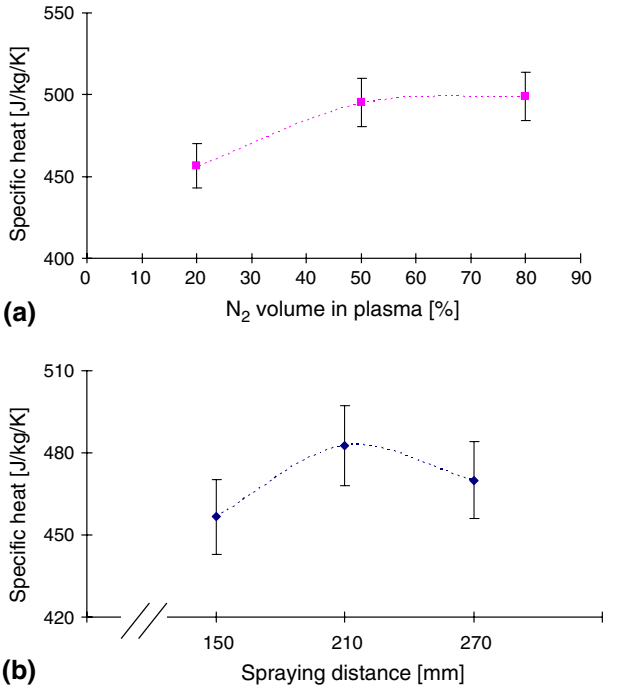

Fig. 13 Specific heat changes vs. (a) N_2 vol.% change in plasma and (b) spraying distance change

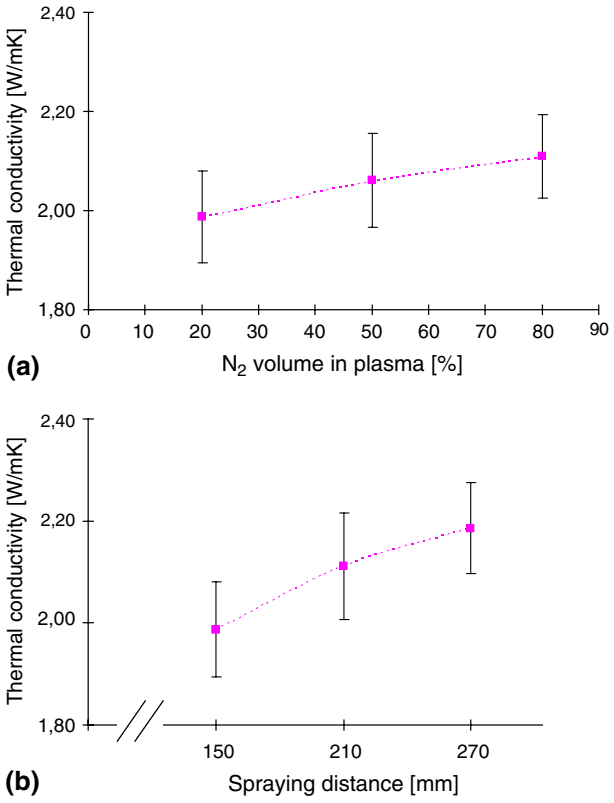

Fig. 12 Thermal conductivity of IPS-N_2 MBTBCs

MBTBCs which it tends to slightly increase with the SD even though the relative porosity increases by 25%. This means that porosity is not a major factor affecting thermal properties of the MBTBCs.

4.6 Thermal Conductivity of MBTBCs

From the C_p and ρ values measured, TC of IPS-N_2 MBTBCs were calculated and plotted in Fig. 12. The lowest TC obtained in this study is 2.0 W/mK. The N_2 vol.% in plasma is not found to influence TC significantly based on the large error reported for these measurement. However, TC increases with larger spraying distance. It can be explained by the specific heat increase, shown in Fig. 13, which is associated with O_2 wt% increase as shown in Fig. 7.

4.7 Anisotropic Properties of MBTBCs

The coating structures of MBTBCs are anisotropic since they are formed by the ''stacking'' of previously molten splats into layers perpendicular to the spray direction. Anisotropic TD was measured in two directions, the laser incident direction a) parallel (PA) and perpendicular (PE) to the spray direction for the TD measurement (see Fig. 2). Calculated TC for the MBTBCs is presented in Table 6.

From the table, it can be noted that the thermal conductivity is a bit lower with the PA types, but it is not very significant so that we may ignore anisotropic thermal property in this MBTBCs study.

Table 6 Thermal diffusivity, density, specific heat, thermal conductivity of anisotropic MBTBCs

Type of MBTBCs	TD, 10^{-7} m²/s	DN, kg/m³	Cp, J/kg/K	TC, W/mK
MBTBCs (IPS-N_2)				
PA	6.30 ± 0.02	6910 ± 95	456 ± 16	2.0 ± 0.13
PE	6.78 ± 0.02	6859 ± 28	470 ± 16	2.2 ± 0.10

Note: MBTBCs used for the anisotropic study are IPS-20% N_2 sprayed with spraying distance of 210 mm.

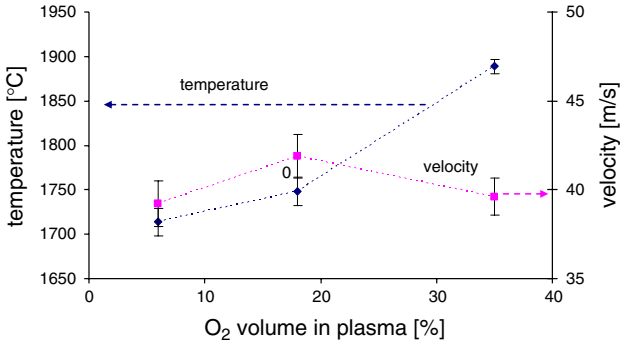

Fig. 14 In-flight particle temperature: (a), and velocity (b) with various O_2 vol.% present in the plasma

5. Induction Plasma Sprayed MBTBCs with O_2 (IPS-O_2)

5.1 In-Flight Particle Characteristics

Figure 14 shows that in-flight particle temperatures increase as the O_2 partial pressure increases in the plasma, while particle velocity remains nearly constant (between 39 and 43 m/s) within the error of the 90% confidence level.

The temperature increase noted can be also explained by the greater amount of exothermic reaction taking place between the O_2 rich plasma and the in-flight molten particles.

5.2 X-Ray Diffraction

The XRD patterns in Fig. 15 show that higher O_2 partial pressure in plasma gas results in more crystalline phases and oxides in the coatings. As illustrated in this Figure, peaks at 2P values of 44.67, 65.02, and 82.33 correspond to the Fe phase (Ref 26), and they become stronger with the increase in O_2 partial pressure in the plasma, indicating that more Fe crystalline phase is present in the MBTBCs. Peaks at 2P values of 35.45, 56.78, and 62.72 correspond to Fe_3O_4 (Ref 27). The oxide is more likely formed in flight because we may ignore oxidation on the substrate due to the low substrate temperature of 200 °C.

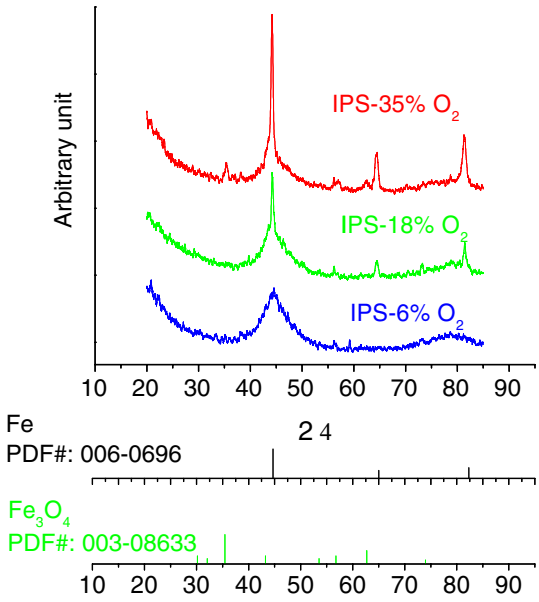

Fig. 15 XRD patterns of MBTBCs, sprayd with O_2 vol.% changes in the plasma

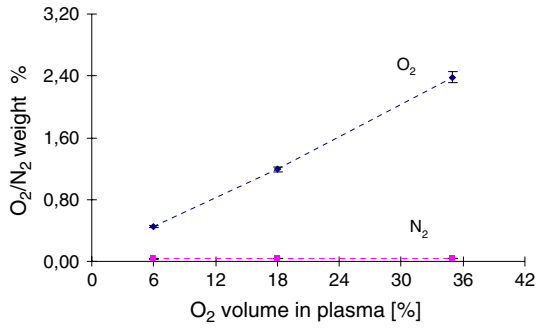

Fig. 16 O_2/N_2 contents in MBTBCs as a function of O_2 vol.% in plasma

5.3 O_2/N_2 Contents

As shown in Fig. 16, the result on O_2/N_2 analysis confirms the XRD data in Fig. 15, which show increased O_2 wt% in the coatings as O_2 vol.% increase in the plasma gas.

5.4 Microstructure, Grain Size, and Porosity

Crystal structure of IPS-O_2 MBTBCs changes from almost fully amorphous to significantly crystalline with O_2 vol.% change in plasma from 6 to 35%, as presented in Fig. 15. Crystalline phases observed in MBTBCs with higher O_2 partial pressures in the plasma may be resulting from the different flattening behaviors with the different oxide contents present in molten particles when they impinge onto a substrate. With greater oxide content in particles, they flatten to lesser extent on impacting the substrate as seen in Fig. 17c), due to the altered wetting behavior discussed in case of IPS-N_2 MBTBCs

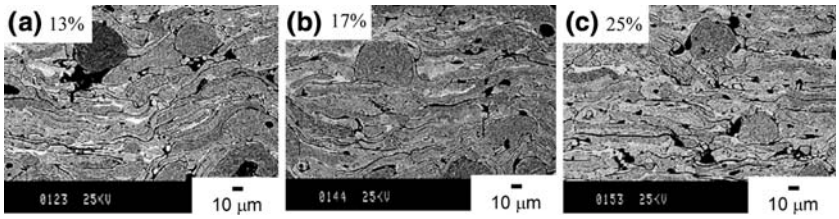

Fig. 17 SEM backscattered images and porosity of MBTBCs sprayed with (a) 6%, (b) 18%, and (c) 35% O_2 vol.% in the plasma

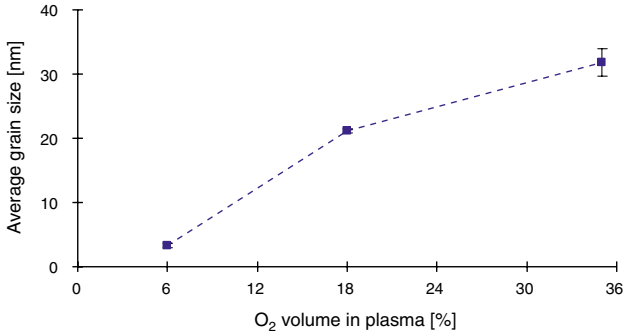

Fig. 18 Grain size changes in MBTBCs, with increased plasma O_2 partial pressure

(Ref 15, 26). Thus the cooling rates of the impinging particles are lower so that the particles have more time to crystallize.

As seen from Fig. 18, the grain size of MBTBCs changes from a few nanometers to few tens of nanometers with O_2 partial pressure increase in the plasma. This is consistent with the lower quenching rate expected at high O_2 pressure.

Increased O_2 partial pressure in the plasma resulted in more pores in the MBTBCs, as presented in Fig. 17. The porosity increases from 13 to 25% with an O_2 vol.% change from 6 to 35% in the plasma, respectively. The increased porosity can be explained by the wetting behavior already discussed.

5.5 Thermal Diffusivity

As shown in Fig. 19, TD of IPS-O_2 MBTBCs increases as O_2 partial pressure increases in the plasma. The increase can be explained by the larger amount of crystalline phase, and grain size increase from a few nanometers to about 30 nm as well as presence of the oxide phase, Fe_3O_4 (magnetite), which has a high thermal conductivity (9.7 W/mK after Ref 28). For the TD increase, porosity effect, changing from 13 to 25%, looks to be outrun by the crystallinity change.

6. Features Affecting Properties of MBTBCs

A matrix of dependent and independent variables summarizes all the results obtained in this study.

As shown in Table 7, MBTBCs with larger SD consist of more O_2 contents which cause higher heat capacity and higher thermal diffusivity (considering O_2 contents as Fe_3O_4) of the coatings resulting in higher TC in MBTBCs. Porosity and density are also changed with SD change but it looks to be outrun.

Higher N_2 partial pressure in IPS plasma gas increases N_2 contents and porosity in MBTBCs. Higher N_2 contents resulted in higher heat capacity of MBTBCs, which increases directly TC of MBTBCs.

O_2 vol.% in plasma gas affects several factors such as O_2 contents, porosity (density), phase, and crystal structure. Higher O_2 contents in the coatings resulted in higher

Table 7 Matrix of features affecting properties of MBTBCs

		Dependent variables									
Independent variables		N_2 contents in coating, wt%	O_2 contents in coating, wt%	Porosity	Density, kg/m^3	Phases	Grain size, nm	Crystal structure	Thermal diffusivity, E-7 m^2/s	Heat capacity, J/kg/K	Thermal conductivity, W/mK
S3 SD, mm	150	0.11	0.11	12	6910	A	3	A	6.30	456	1.99
S4	210	0.09	0.15	13	6779	A	3	A	6.45	482	2.11
S5	270	0.07	0.14	15	6701	A	3	A	6.78	485	2.20
S3 IPS with N_2 vol.%	20	0.11	0.11	12	6910	A	3	A	6.30	456	1.99
S2 change in plasma	50	0.12	0.10	14	6620	A	3	A	6.29	495	2.06
S1	80	0.12	0.10	16	6590	A	3	A	6.41	498	2.10
S6 IPS with O_2 vol.%	6	0.3	0.45	13	6715	A	3	A	7.52	496	2.50
S7 change in plasma	18	0.3	0.19	17	6571	Fe	21	A + N	9.06	488	2.91
S8	35	0.4	2.38	25	6198	Fe & Fe_3O_4	32	A + N	9.97	497	3.07

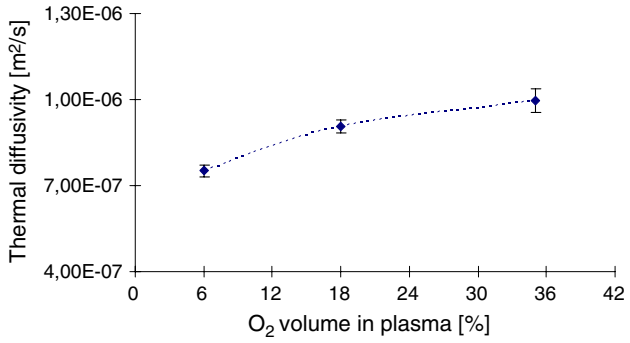

Fig. 19 Thermal diffusivity changes vs. O_2 vol.% change in plasma gas

porosity (lower density), precipitation of a new phase Fe_3O_4, and crystal structure change from amorphous to a mixture of amorphous and nanostructure. In this case, Fe_3O_4 phase and the mixed crystal structure are dominant factors contributing to the higher TD and TC of MBTBCs.

7. Conclusions

The key experimental observations are listed below:

1. High TC of metallic-based materials was reduced by engineering of amorphous and nanocrystalline structure of MBTBCs using IPS technology.
2. The measured TC of MBTBCs was found to be as low as 2.0 W/mK, and this low TC was likely obtained from the increased phonon scattering by use of engineered amorphous structures in the coatings so that the phonon contribution to the total TC was reduced.

In summary, we may conclude that thermal properties of MBTBCs are mainly governed by two factors, such as phases and crystal structure or grain size. There are also hidden factors, such as interlamellar contact, splat thickness, the ratio between molten/unmolten numbers of particles in the coatings, and crack lengths, which should be considered to complete the correlation between the dependent and independent variables. The study of those factors is to be remained for future work.

Acknowledgment

NCE (Network of Center of Excellence in Canada) has fully supported this work under Auto21 program with the project code of C11-C00.

References

1. W.D. Kingery, H.K. Bowen, and D.R. Uhlmann, Introduction to Ceramics, Chapter 12, 2nd ed. NY, USA: John Wiley & Sons, 1976
2. A.J. Slifka, B.J. Filla, J.M. Phelps, G. Bancke, and C.C. Berndt, Thermal Conductivity of a Zirconia Thermal Barrier Coating. *J. Therm. Spray Techn.*, 1998, **7**(1), p 43-46
3. K.W. Schlichting, N.P. Padture, and P.G. Klemens, Thermal Conductivity of Dense and Porous Yttria Stabilized Zirconia. *J. Mat. Sci.*, 2001, **36**, p 3003-3010
4. D. Shin, F. Gitzhofer, and C. Moreau, Development of Metal based Thermal Barrier Coatings for Low Heat Rejection Diesel Engines, Proceedings of ITSC 2005, May 2-3, Basel in Swiss
5. S. Kumar and G.C. Vradis, Thermal Conductivity of Thin Metallic Films. *Trans. ASME*, 1994, **116**, p 28-34
6. P.G. Klemens, Theory of Thermal Conductivity of Nano-Phase Materials. Chemistry and Physics of Nanostructures and Related Non-Equilibrium Materials, 1997, p 97-104
7. P.G. Klemens and M. Gell, Thermal Conductivity of Thermal Barrier Coatings. *Mat. Sci. Eng. A*, 1998, **245**, p 143-149
8. S. Raghavan, W. Hsin, R.B. Dinwiddie, W.D. Porter, and M.J. Mayo, The Effect of Grain Size, Porosity and Yttria Content on the Thermal Conductivity of Nanostructured Zirconia. *Scripta Mater.*, 1998, **39**(8), p 1119-1125
9. P.G. Klemens, Phonon Scattering by Oxygen Vacancies in Ceramics. *Physica B*, 1999, **263-264**, p 102-104
10. H.-S Yang, J.A. Eastman, L.J. Thomson, and G.R. Bai, Grain-Size-Dependent Thermal Transport Properties in Nanostructured Yttria-Stabilized Zirconia. *Mater. Res. Soc. Sympos. Proc.*, 2002, **703**, p 179-184
11. D.J. Branagan, Formation of Metallic Thermal Barrier Alloys, US Patent US2005/0013723 A1, Jan. 20, 2005
12. J. Blain, F. Nadeau, L. Pouliot, C. Moreau, P. Gougeon, and L. Leblanc, Integrated Infrared Sensor System for Online Monitoring of Thermally Sprayed Particles. *Surface Eng.*, 1997, **13**(5), p 420-424
13. D. Shin, F. Gitzhofer, and C. Moreau, Influence of Induction Plasma Gas Composition on Ti Coatings Microstructure and Composition, Proceedings of ITSC 2004, May 2004 Osaka in Japan
14. H.P. Klug, L. E. Alexander X-ray Diffraction Procedures. John Wiley & Sons, NY, USA, 1974
15. B. D. Cullity, Elements of X-ray Diffraction, 2nd ed., in Korean Version, Translated by Han B.H., Bando Publishing Co. Ltd. Korea, 1990
16. T. Haraguchi, K. Yoshimi, H. Kato, S. Hanada, and A. Inoue, Determination of Density and Vacancy Concentration in Rapidly Solidified FeAl Ribbons. *Intermetallics*, 2003, **11**, p 707-711
17. ''Standard Test Method for Density Determination for Powder Metallurgy Materials Containing Less than Two Percent Porosity'', B 31-93, Annual Book of ASTM Standards
18. ''Standard Test Method for Density of Glass by Buoyancy'', C 693-93, Annual Book of ASTM Standards
19. ''Standard Test Method for Density of High-Modulus Fibers'', D 3800-99, Annual Book of ASTM Standards
20. W.J. Parker, R.J. Jenkins, C.P. Butler, and G.L. Abbott, Flash Method of Determining Thermal Diffusivity, Heat Capacity and Thermal Conductivity. *J. Appl. Phys.*, 1961, **32**(9), p 1679-1684
21. Design-Expert version 6.0.1 State-Ease Inc. Minneapolis, MN, USA
22. SHS717 MSDS Data sheet, the Nanosteel Company
23. W.G. Moffatt, The Handbook of Binary Phase Diagrams. Schenectady, NY, 1976
24. R.H. Perry and D.W. Green, Perry's Chemical Engineers' Handbook, 1999, McGraw-Hill Companies. Inc
25. M. Fukumoto, K. Hamada, and M. Shiba, Dependence of Thermal Sprayed Particle/Substrate Interface Microstructure on Substrate Temperature. *Proc. Int. Thermal Spray Conf.*, 2003, **2**, p 1047-1052
26. H.F. Swanson, PDF file # 06-0694, *Natl. Bur, Stand. U.S. Circ.*, 1955, **20**, p 539
27. G.A. Harcourt, PDF File # 03-0863, *Am. Mineral.*, 1942, **27**, p 90
28. CES Selector 4.1, Granta Design Limited, Rustat House, 62 Clifton Road, Cambridge, CB1 7EG, UK